THE JOURNAL OF PHYSICAL CHEMISTRY B
A JOURNAL OF THE AMERICAN CHEMICAL SOCIETY

pubs.acs.org/JPCB

Article

Concentration Dependence of Dynamics and Structure among Hydrated Magnesium Ions: An Ultrafast Infrared Study

Samantha T. Hung, Sean A. Roget, Weizhong Zheng, and Michael D. Fayer*

Cite This: J. Phys. Chem. B 2023, 127, 3278−3290

Read Online

ACCESS | Metrics & More | Article Recommendations | Supporting Information

ABSTRACT: The dynamics of aqueous magnesium chloride solutions, from relatively dilute (0.5 m) to near saturated (4.2 m) concentrations, were investigated using ultrafast two dimensional infrared and polarization selective pump-probe spectroscopies. The experiments were performed on two spectrally distinct nitrile stretch frequencies of the selenocyanate vibrational probe, corresponding to the CN nitrogen lone pair being associated with water and with Mg^{2+}. No chemical exchange of the two species was observed over the experimental time scale (~100 ps), enabling straightforward analysis of their dynamics. The dynamics reported by the Mg^{2+}-associated peak are slower than those of the water-associated peak, suggesting that the immediate environment of the hydrated Mg^{2+} is different from the rest of the solution. Notably, the Mg^{2+}-associated peak displays three spectral diffusion time scales, the slowest being ~30 ps, while the water-associated peak decays as a faster biexponential. From the complete orientational relaxation time and hydrodynamic theory, a magnesium hydration number of six was obtained, which is in good agreement with NMR and X-ray diffraction studies. This hydration number holds for all concentrations until near saturation, when the linewidths and the dynamics deviate from linear trends, indicative of Mg^{2+} solvation structure changes resulting from a shortage of water molecules needed for full solvation.

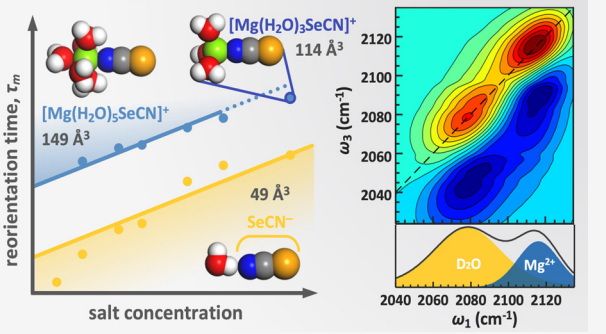

I. INTRODUCTION

The behavior of magnesium ions in water is relevant to processes as varied as vaccine stabilization,[1−3] energy storage,[4−6] and wastewater treatment.[7,8] The physiological and ecological roles of magnesium, which is the most common divalent cation in intracellular fluids and in seawater, are closely linked to its solvation structure and intermolecular interactions.[9−17] The hydration structure of aqueous magnesium chloride ($MgCl_2$) solutions has been studied experimentally by dielectric relaxation spectroscopy,[18] neutron diffraction,[19] Raman spectroscopy,[20] and X-ray measurements.[21−25] While the dynamics of aqueous salt solutions have been investigated with ultrafast infrared spectroscopies, they are often studied using the hydroxyl (OD or OH) stretch of water,[26−29] which, while being an intrinsic part of the solvent system, generally has a vibrational lifetime of <5 ps, limiting the experimental window to relatively fast dynamics. Works by Gaffney and co-workers extended the experimental window to tens of picoseconds by using a thiocyanate (SCN^-) vibrational probe to explore its equilibrium dynamics (40−100 ps) in divalent cation salt solutions.[30−32] However, only cursory details on the rotational and spectral diffusion dynamics of the cation and water bound SCN^- species were provided, as they were complicated by chemical exchange processes.

More recently, Yuan et al. used the CN stretch of methyl thiocyanate (MeSCN) to study the dynamics of concentrated aqueous lithium chloride (LiCl) solutions using two-dimensional infrared (2D IR) spectroscopy.[33,34] The two overlapping dynamical contributions from the MeSCN species with nitrogen lone pairs bound to the cation and to water were separated using 2D Gaussian modeling and the effects of chemical exchange were removed with kinetic modeling. In general, the dynamics slowed with increasing salt concentration, which was also observed in another study of LiCl solutions at the same concentrations but probed on shorter time scales with the OD stretch of HOD.[29] Like the water- and cation-associated MeSCN, there are two OD populations: water- and anion-associated. However, the broad OD linewidths led to complete spectral overlap of the two species; only the dynamics of the chloride-associated OD with a longer vibrational lifetime (5.5 versus 1.2 ps) were presented. A long spectral diffusion time scale of ~40 ps that was observed by

Received: January 13, 2023
Revised: March 7, 2023
Published: March 30, 2023

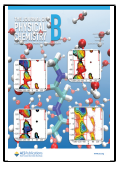

https://doi.org/10.1021/acs.jpcb.3c00300
J. Phys. Chem. B 2023, 127, 3278−3290

both MeSCN probe populations was not observed by the OD probe. Besides this difference in dynamics reported by different vibrational probes, the cation- and water-associated MeSCN also experience different rotational dynamics. In a separate study of dynamics in aqueous monovalent and divalent salt solutions using the OD probe, the valency of the cation influenced the dynamics sensed by the halide-associated OD probe.[28]

To expand understanding of aqueous salt solutions containing a high charge density cation, we studied the structure and dynamics in aqueous solutions of a common magnesium salt, $MgCl_2$, with concentrations spanning 0.5 to 4.2 molal. Femtosecond infrared polarization selective pump-probe (PSPP) and two-dimensional infrared (2D IR) experiments were conducted using the nitrile (CN) stretching mode of a selenocyanate ($SeCN^-$) vibrational probe. The $SeCN^-$ probe was chosen as it was proven to be a reliable probe of ultrafast water dynamics in deuterated water (D_2O), giving almost identical spectral diffusion time scales as a native hydroxyl probe.[35] The long $SeCN^-$ vibrational lifetime (20−40 ps), large transition dipole, and substantial solvatochromism[36−39] in $MgCl_2$ solution facilitate the measurement of a broad range of time scales and the detection of diverse and changing solvent structures.

In this study, we elucidated the vastly different spectral and dynamical characteristics of the two $SeCN^-$ probe populations: Mg^{2+}- and D_2O-associated. Similarly disparate dynamics of selenocyanate in free form and covalently bound to the cation of a room temperature ionic liquid (RTIL) are considered in the interpretation of the results.[40] Since hydrated magnesium cations are expected to have octahedral coordination, as shown by proton NMR[41,42] and X-ray diffraction studies,[23,43] and long, microsecond water residence time,[44] the rotational dynamics for the Mg^{2+}-associated $SeCN^-$ are explored in terms of a long-lived Mg^{2+} coordination sphere within the framework of a wobbling-in-a-cone model[45−48] and hydrodynamic theory. The line shapes and spectral diffusion dynamics are considered in terms of changing ion and water arrangements,[49] as well as charge transfer effects in the binding of the high charge density Mg^{2+} cation.[50]

II. EXPERIMENTAL METHODS

II.A. Sample Preparation and Linear IR Spectroscopy. Magnesium chloride ($MgCl_2$, anhydrous, >98%) purchased from Sigma Aldrich and deuterated water (D_2O, 99.9% D) purchased from Cambridge Isotope Laboratories were used without further treatment. Potassium selenocyanate (KSeCN, 99%) from Acros Organics was vacuum dried under heat (<100 mTorr, 60 °C) and stored in a nitrogen glovebox.

Different concentrations of the aqueous solutions with Mg^{2+} to D_2O mole ratios of 1−12, 1−16, 1−20, 1−30, 1−40, and 1−100 were prepared gravimetrically and syringe filtered (0.22 μm). The densities and kinematic viscosities of the solutions were measured using a 5 mL pycnometer and a calibrated Cannon-Ubbelohde viscometer, respectively. The solution densities, dynamic viscosities, and concentrations are tabulated in Table S1 of the Supporting Information (SI). The 1−12 mole ratio solution is near saturation and corresponds to 4.2 m and 4.1 M. The 1−100 solution corresponds to 0.5 m and 0.5 M.

The vibrational probe, KSeCN, was added at a 0.25 m concentration to the filtered salt solution, and the resulting solution was syringe filtered again to yield an optically clear solution. The solutions were sandwiched between two 25 mm-diameter, 3 mm-thick CaF_2 windows, and the optical path length was set with a 25 μm Teflon spacer between the windows. Linear IR spectra of the samples with and without the vibrational probe were taken with a Thermo Scientific Nicolet iS50 spectrometer purged with air free of CO_2 and H_2O.

Sample evaporation was negligible for the 1−12 and 1−16 solutions, which produced identical linear spectra before and after experiments. For concentrations at and below 1−20, the linear spectra and measured dynamics changed dramatically over the span of hours. These samples were sealed in paraffin wax as follows: after sample cell assembly, circular stickers with diameters just larger than that of the exposed CaF_2 windows were applied on the sample cell over the recessed windows. Then, the sample cell was submerged in melted wax (~60 °C) for about 30 s. Excess wax and the stickers were removed after the wax cooled. These sealed samples last for about a week.

II.B. Nonlinear IR Spectroscopy. The spectrometer used for the polarization selective pump-probe (PSPP) and two-dimensional infrared (2D IR) vibrational echo experiments is configured in a pump-probe geometry as previously described in detail.[51] Briefly, a 1 kHz repetition rate, 800 nm Ti:Sapphire oscillator/regenerative amplifier system pumps an optical parametric amplifier to generate ~7 μJ mid-IR pulses centered at 2096 cm^{-1} with ~170 fs full width at half-maximum (FWHM) duration. The mid-IR pulse is split into a strong pump pulse and a weak probe pulse with a ZnSe beam splitter. The pump pulse is directed into a germanium acousto-optic pulse shaper, which allows for precise control over the number, amplitudes, phases, and relative timing of outgoing pump pulse(s).[51−53] The probe pulse is sent into a precision mechanical delay stage, which controls the timing of the probe relative to the pump.

For the PSPP experiments,[54,55] a pump pulse polarized at 45° relative to the horizontally polarized (0°) probe pulse is chopped at half the laser repetition rate. The probe pulse meets the sample at a variable time delay t after the pump pulse. The transient intensity differences in the probe are resolved at 45° and −45° following the probe's transmission through the sample, corresponding to directions parallel and perpendicular to the pump. The polarization resolved transient absorptions track the changing projections of the reorienting probe molecules, giving time-dependent parallel $S_{\parallel}(t)$ and perpendicular $S_{\perp}(t)$ signals. Immediately before the spectrograph, both signals are projected back to the horizontal polarization to avoid distortions due to different polarization dependent grating efficiencies. The spectrally dispersed frequencies are then detected on a mercury cadmium telluride (MCT) array detector.

In the 2D IR experiment,[56,57] two collinear pump pulses and a probe pulse interact sequentially with the sample. The emission of a third-order vibrational echo signal in the direction of the probe pulse is stimulated by the probe pulse, which also acts as a phase-locked local oscillator for heterodyne detection. Pulses 1 and 2 are separated by τ and initiate the first coherence and population periods, respectively, to label and store the initial frequencies, ω_1, of an ensemble of excited vibrational probes. Individual probe molecules exhibit different vibrational frequencies within an inhomogeneously broadened absorption line due to varying molecular interactions with the local solvent structure. Pulse 3 marks the end of a variable waiting time T_w, initiating the second coherence period to read

https://doi.org/10.1021/acs.jpcb.3c00300
J. Phys. Chem. B 2023, 127, 3278−3290

out the final frequencies, ω_3. As the liquid structure surrounding a probe molecule changes over T_w, so do its interactions with the probe molecule, causing the probe molecule to sample a range of vibrational frequencies. For a 2D spectrum at a given T_w, the heterodyned signal is frequency dispersed by a spectrograph to yield the ω_3 axis. At each ω_3 frequency, the interferograms produced by scanning τ are recorded and numerically Fourier transformed to yield the ω_1 axis in the 2D spectrum. At early T_w, structural evolution has had little time (T_w) to occur, so ω_3 and ω_1 are strongly correlated, giving an elongated 2D spectrum along the $\omega_3 = \omega_1$ diagonal. With increasing T_w, more solvent configurations have been sampled, so ω_3 and ω_1 become increasingly decorrelated, resulting in an increasingly round band shape.

III. RESULTS AND DISCUSSION

III.A. Linear IR Absorption Spectra. Background subtracted linear absorption spectra of $SeCN^-$ in aqueous $MgCl_2$ solutions of varying concentrations and in pure D_2O are shown in Figure 1a. There are two peaks in the $MgCl_2$ solution

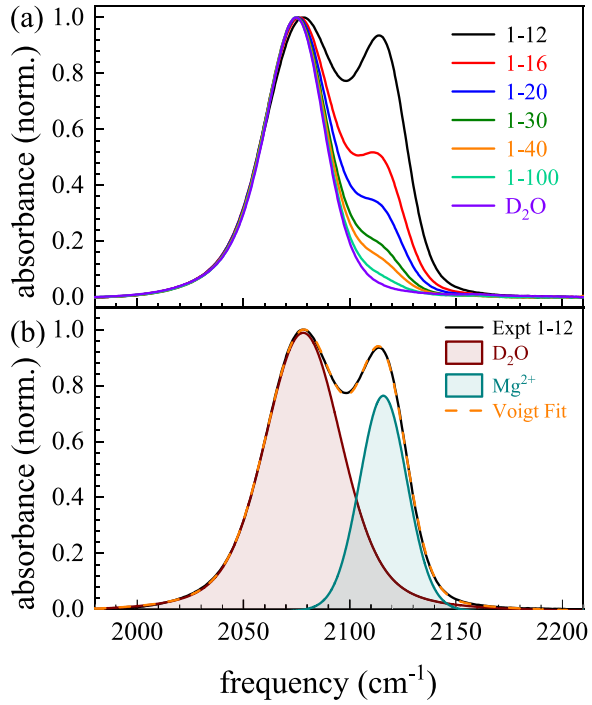

Figure 1. (a) Linear IR spectra of the CN stretch of $SeCN^-$ in D_2O solutions of varying $MgCl_2$ concentrations and in pure D_2O (purple curve). The D_2O-associated peak is centered at ~2075 cm^{-1}. The higher frequency peak that grows in with increasing salt concentration centered at ~2115 cm^{-1} is the Mg^{2+}-associated peak. (b) The 1−12 spectrum (black curve) was fit (dashed orange curve) with two Voigt line shapes to determine the characteristics of the two underlying contributions, the D_2O-associated (burgundy) and Mg^{2+}-associated (cyan) peaks.

spectra and they fit well to two Voigt line shapes (Figure 1b, for 1−12 mole ratio). The lower frequency peak at ~2075 cm^{-1} is the D_2O-associated $SeCN^-$ (burgundy peak in Figure 1b, hereinto referred to as the "D_2O peak"). A blue-shifted peak at ~2115 cm^{-1} grows in with increasing $MgCl_2$ concentration. This higher frequency peak is the Mg^{2+}-associated $SeCN^-$ (cyan peak in Figure 1b, hereinto referred to as the "Mg^{2+} peak"), similar to the blue-shifted Mg^{2+}-associated SCN^- peak in $MgCl_2$ D_2O solutions.[30−32]

The center frequencies and FWHM of the two peaks are tabulated in Table 1. The D_2O peak blue shifts from 2074.7 to 2078.1 cm^{-1} and broadens with increasing salt concentration, from a FWHM of 32.9 cm^{-1} in pure D_2O to 43.3 cm^{-1} in the saturated (1−12) $MgCl_2$ solution. The Mg^{2+} peak also broadens with increasing concentration, from a FWHM of 15.2 cm^{-1} in the 1−40 solution to 26.4 cm^{-1} in the 1−12 solution. The center and FWHM of the Mg^{2+} peak for the lowest concentration (1−100, turquoise spectrum in Figure 1a) cannot be resolved. In the concentration range analyzed, the Mg^{2+} center frequency varies within ~1 cm^{-1}, and the slight variation may be a result of small fitting errors due to the slight asymmetry of the D_2O peak.[35]

Generally, the vibrational frequency of the nitrile stretch of an $SeCN^-$ with multiple hydrogen bonds (H-bonds) are red-shifted with respect to an $SeCN^-$ with only a single interaction.[58] In D_2O, the first H-bond, collinear with the CN, tends to be stronger, leading to a blue shift, while weaker, off axis H-bonds that form subsequently result in red shifts.[35] As discussed later in Section III.D, the $SeCN^-$ associated with Mg^{2+} is bound within the first coordination shell of the hexa- or tetra-coordinated Mg^{2+} cation, rendering the $SeCN^-$ less accessible for additional H-bonds. The ~40 cm^{-1} blue shift of the Mg^{2+} peak relative to the D_2O peak is in part a result of fewer H-bonds, and also the high charge density of Mg^{2+}. Electron density shifts in the nitrile-cation contact ion pair increase the CN triple bond character (vs double bond), resulting in blue shifts of the vibrational frequency.[30−32,58] The magnitude of this blue shift increases with cation charge density. The lack of frequency change for the Mg^{2+} peak with concentration indicates that the net environment (average interactions) sensed by the spatially hindered $SeCN^-$ does not vary significantly with concentration.

The blue shift of the D_2O peak center frequency with increasing concentration suggests an increase in D_2O−CN H-bond strength. With increasing salt concentration, fewer water molecules solvate the ionic species (Mg^{2+}, Cl^-, and $SeCN^-$). A molecular dynamics study shows that the proportion of free ions (i.e., no counter ions for multiple hydration layers) in aqueous $MgCl_2$ solution decays to zero at about 1 M (comparable to 1−40).[49] The proportion of solvent-separated ion pairs (ion pairs separated by two water molecules) peaks at about 0.5 M (1−100) and then decays. The solution is dominated by solvent-shared ion pairs (ion pairs separated by one water molecule) by 3.5 M (comparable to 1−16). From the perspective of water, fewer waters are surrounded by other waters and are instead adjacent to ions. Charge transfer processes described in a quantum mechanical study result in a small positive charge among the waters beyond the first coordination shell of Mg^{2+}.[50] The H-bonds of these partially positively charged waters to the CN are expected to become stronger and the CN center frequency bluer as the Mg^{2+} cation becomes increasingly prevalent and proximate.

The overall linewidth, which increases monotonically with increasing concentration for both peaks (FWHM in Table 1), contains homogeneous and inhomogeneous contributions.[57] These contributions are indistinguishable in the linear spectra but can be determined from the 2D spectra (discussed below in Section III.E). Homogeneous broadening affects each molecule in an ensemble of probe molecules in the same way and gives the intrinsic minimum linewidth (resulting from

https://doi.org/10.1021/acs.jpcb.3c00300
J. Phys. Chem. B 2023, 127, 3278−3290

Table 1. Line Shape Parameters and Vibrational Lifetimes

	D_2O-associated			Mg^{2+}-associated		
concentration (mole ratio)	center (cm^{-1})	FWHM (cm^{-1})	lifetime (ps)	center (cm^{-1})	FWHM (cm^{-1})	lifetime (ps)
1−12	2078.1 ± 0.1	43.3 ± 0.1	23.5 ± 0.4	2115.8 ± 0.1	26.4 ± 0.1	30.1 ± 0.3
1−16	2076.2 ± 0.2	40.3 ± 0.2	25.0 ± 0.3	2114.9 ± 0.1	24.7 ± 0.2	29.9 ± 0.1
1−20	2075.4 ± 0.1	38.6 ± 0.1	26.3 ± 0.8	2114.9 ± 0.1	22.7 ± 0.4	29.8 ± 0.6
1−30	2074.7 ± 0.1	36.8 ± 0.2	28.0 ± 0.9	2115.4 ± 0.2	19.0 ± 0.3	30.2 ± 0.5
1−40	2074.4 ± 0.1	35.8 ± 0.1	30.6 ± 0.7	2115.8 ± 0.1	15.2 ± 0.4	31.3 ± 0.7
1−100[a]	2074.3 ± 0.1	35.4 ± 0.1	32 ± 1			32.0 ± 0.7
D_2O[35]	2074.7 ± 0.1	32.9 ± 0.1	36.2 ± 0.1			

[a]The Mg^{2+}-associated peak is too small to reliably extract the center frequency and FWHM.

phase-randomizing collisions, vibrational relaxation, and orientational relaxation). Inhomogeneous broadening arises from variability in the solvent structure in the vicinity of the probe molecule. As individual molecules are in distinct environments, they experience varying probe−solvent intermolecular interactions, resulting in a range of vibrational transition energies. The overall line shape is then the superposition of many homogeneously broadened line shapes with slightly different center frequencies.

In Figure 2a,b, the homogeneous linewidths (gray) for both the D_2O and Mg^{2+} peaks are shown to be within error of the average value across concentrations (shaded gray region). Given this, the increase in the overall linewidths (dark pink) with increasing concentration is primarily due to the increase in the inhomogeneous linewidths (green). Greater inhomogeneous broadening arises from a greater variety of water−CN and cation−CN interactions resulting from the increasing variation in the solvent configurations (e.g., ion pair configurations such as free and solvent-separated) with increasing salt concentration and ultimately yields a broader distribution of vibrational frequencies.

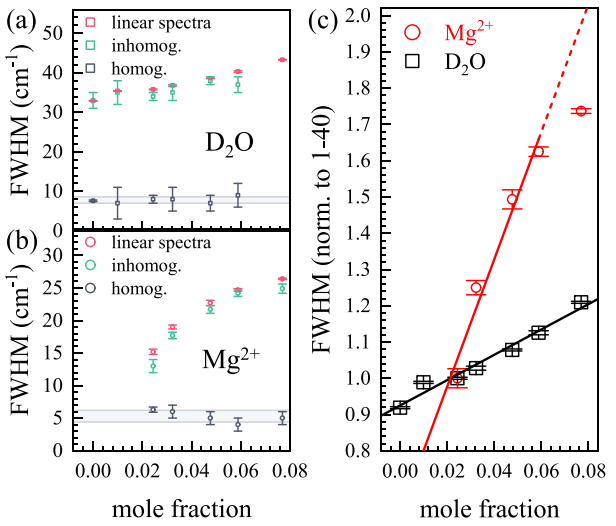

Figure 2. (a, b) Plots of the overall (from linear spectra), inhomogeneous, and homogeneous linewidths (FWHM) for the (a) D_2O and the (b) Mg^{2+} peaks versus mole fraction ($MgCl_2$ in D_2O). The shaded gray regions represent the average homogeneous linewidths averaged over all concentrations with error bars. (c) Plot of the FWHM normalized to the corresponding values at the 1−40 concentration (0.024 mole fraction). The solid lines are linear fits to the data. For the Mg^{2+} peak, the fit is to the lower concentrations (1−40 to 1−16), which extends (dashed line) above the highest concentration data point (1−12, 0.077 mole fraction).

Plotted in Figure 2c are the D_2O and Mg^{2+} FWHM (overall linewidth) normalized to corresponding values at the 1−40 concentration, the lowest concentration for which data was available for both peaks. Linear fits to the D_2O FWHM (black line) and the Mg^{2+} FWHM for the lower concentrations (red line, fit for concentrations 1−40 to 1−16) are presented as guides for the eye for comparing the monotonic FWHM increases with concentration. The relative increase in FWHM is greater for Mg^{2+} than for D_2O. The increase is substantially less for the highest concentration point, the 1−12 mole ratio (0.077 mole fraction). This point lies well below the line extended from the fit.

This Mg^{2+} FWHM dependence on concentration is similar to those of other observables in aqueous $MgCl_2$ solutions, including the peak area of the Mg^{2+}−O_{water} Raman stretch,[20] the speed of sound,[59] and the apparent molal volume.[60] Following a roughly linear dependence on concentration at dilute conditions, at concentrations roughly between 1−16 and 1−12 (0.059 and 0.077 mole fractions), the values of these other observables dip below the line extended from fits to the lower concentration data. This concentration range (1−16 to 1−12) is also where solvent-shared ion pairs become the sole ion pair species.[49]

The deviations from linearity of the various observables were attributed to a distinct change in the primary hydration shell, as the low availability of water molecules decreases the cation hydration number.[20,59] In general, the hydrated Mg^{2+} cation does not have a full 2+ charge due to charge transfer propagated through its first solvation shell to the surrounding waters (these waters acquire a small positive charge).[50] In highly concentrated solutions, the first shell has fewer waters, and the Mg^{2+} begins sharing waters with chloride ions rather than other waters. Thus, the interactions between $SeCN^-$ and Mg^{2+} may strengthen, but the net effects of other Mg^{2+} cations may be weakened due to electrostatic shielding from the nearby chlorides. The result is that the $SeCN^-$ bound to Mg^{2+} becomes less sensitive to concentration changes. The fact that the D_2O linewidth steadily increases while the increase in the Mg^{2+} linewidth slows at high concentrations is experimental evidence that the nonlinear changes in other observables are associated with the cation. The different trends in the D_2O and Mg^{2+} line shapes are also manifested in their dynamics, as discussed below.

III.B. Vibrational Relaxation. The CN stretch vibrational lifetimes of the D_2O- and Mg^{2+}-associated $SeCN^-$ were obtained from the isotropic pump-probe decays $P(t)$ (plotted in the SI, Figure S1), which were constructed from the parallel and perpendicular signals of the pump-probe experiments:[54,55]

https://doi.org/10.1021/acs.jpcb.3c00300
J. Phys. Chem. B 2023, 127, 3278−3290

$$P(t) = [S_{\parallel}(t) + 2S_{\perp}(t)]/3 \quad (1)$$

For the D_2O peak, the typically used 0−1 transition (centered ∼2075 cm^{-1}) overlaps completely with the 1−2 transition of the Mg^{2+} peak (centered ∼2085 cm^{-1}). The 1−2 transition is the excited vibrational state absorption, which is shifted by the vibrational anharmonicity to lower frequencies (e.g., from 2115 to 2085 cm^{-1} for the Mg^{2+} peak). To extract the lifetimes of only the $SeCN^-$ associated with D_2O, the red side of the D_2O-associated 1−2 transition (i.e., <2045 cm^{-1}) was analyzed. The $P(t)$ decays are biexponential due to the presence of a fast spectral diffusion component in addition to vibrational relaxation, as previously observed in $SeCN^-$ in D_2O.[35] The non-Condon effect, i.e., frequency-dependent transition dipoles, results in non-uniform pumping of the absorption line that equilibrates on the time scale of spectral diffusion.[35,61] Spectral diffusion is discussed in detail in Section III.E. The second, longer time constant is the vibrational lifetime. Fitting the $P(t)$ with a single exponential from 10 ps onward to avoid the fast spectral diffusion yields the same lifetime (i.e., the time constant is the same as the second time constant of the biexponential fit). The frequency independent lifetime (Table 1) decreases monotonically with increasing salt concentration, from 36.2 ps in pure D_2O to 23.5 ps in the 1−12 solution. The vibrational lifetime measures how rapidly the excited $SeCN^-$ dissipates vibrational energy through solvent-assisted intramolecular vibrational energy redistribution from the excited CN stretch to other $SeCN^-$ modes (e.g., C-Se stretch and SeCN bend) and through intermolecular vibrational energy relaxation to solvent modes.[37,62,63] The stronger probe−solvent interactions (the interactions between $SeCN^-$ with the waters that become slightly positively charged in the presence of the Mg^{2+} cations) that led to the blue shift in the CN center frequency may also accelerate the vibrational relaxation by making energy transfer to the solvent modes more efficient.[63−65]

For the Mg^{2+} peak, long time offsets were observed in the pump−probe signals. The treatment of this offset and determination of the Mg^{2+} lifetime are described in the SI. The frequency-independent lifetime obtained (Table 1) varies between ∼30 and 32 ps for all concentrations. Given the overlapping error bars, it may not be definitive to examine a trend. However, given this caveat, the lifetimes also decrease—albeit slightly—with increasing concentration like the D_2O peak but plateaus upon reaching the critical concentrations of 1−16 to 1−12. Compared to the D_2O bound species, both the center frequency and the vibrational lifetime of $SeCN^-$ bound to and strongly interacting with Mg^{2+} are less affected by the increasing presence of other Mg^{2+} cations.

III.C. Orientational Relaxation. The direct extraction of the vibrational and orientational relaxation time scales of $SeCN^-$ associated with D_2O and Mg^{2+} from the pump-probe experiment was possible due to spectral separation of the two species and chemical exchange that is very slow compared to the observables (see Section III.E). Using the 0−1 Mg^{2+} transition and 1−2 D_2O transition enabled spectral separation, as discussed above in connection with the determination of $P(t)$. The dynamics obtained from the D_2O 1−2 transition are identical to those obtained from the 0−1 transition[30,31] and was confirmed to be the case for the pure D_2O solution, which has no interfering Mg^{2+} peak.

The orientational anisotropy $r(t)$ is constructed using the following equation, where $C_2(t)$ is the second-order Legendre polynomial orientational correlation function of the transition dipole moment:[54,55]

$$r(t) = \frac{S_{\parallel}(t) - S_{\perp}(t)}{S_{\parallel}(t) + 2S_{\perp}(t)} = 0.4C_2(t). \quad (2)$$

In principle, at t = 0 ps, before any orientational relaxation has occurred, $C_2(t)$ = 1 and $r(t)$ = 0.4. However, deviations from the $r(t)$ value of 0.4 are common due to subpicosecond inertial motions that are too fast to resolve.[66]

The $SeCN^-$ $r(t)$ decay curve in pure D_2O is a biexponential with t_1 = 1.4 ps and t_2 = 4.5 ps. For all concentrations of the $MgCl_2$ solutions, the D_2O $r(t)$ decays (Figure 3a) fit well to

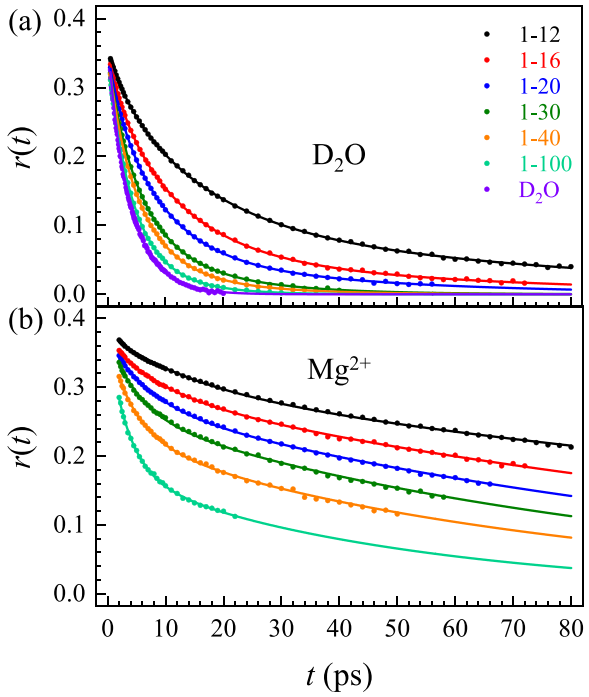

Figure 3. Measured rotational anisotropy $r(t)$ decays of $SeCN^-$ in D_2O solutions of varying $MgCl_2$ concentrations and in pure D_2O. (a) The solid curves are multiexponential fits to the data for the D_2O peak. (b) The solid curves are two-component fits to the data at the center frequency of the Mg^{2+} peak.

triexponentials with no offsets (Table 2) and are frequency independent. The 1−100 solution has the same first two time constants as pure D_2O, but with lower amplitudes. An additional third time constant t_3 = 8.3 ps contributes ∼30% of the total amplitude. All three time constants then increase monotonically with increasing concentration. The 1−12 solution has t_1 = 2.7, t_2 = 13.5, and t_3 = 67 ps. The amplitude distribution of the three time components does not change significantly with concentration, suggesting that the types of processes governing the rotation of $SeCN^-$ associated with D_2O are similar in all concentrations, but all processes slow with increasing salt concentration.

At each measured frequency of the Mg^{2+}-associated $r(t)$ decays, there are two $r(t)$ contributions due to interference from the broad D_2O 0−1 peak, which partially overlaps with the Mg^{2+} 0−1 peak. The two contributions can be separated using a two-component model of the measured anisotropy (eq S1),[67] which is presented in detail in the SI. Because the D_2O decays are known, it is straightforward to obtain the Mg^{2+}

https://doi.org/10.1021/acs.jpcb.3c00300
J. Phys. Chem. B 2023, 127, 3278−3290

Table 2. Orientational Relaxation Parameters[a]

sample		A_1	t_1 (ps)	A_2	t_2 (ps)	A_3	t_3 (ps)
D_2O	1−12	0.03 ± 0.01	2.7 ± 0.1	0.20 ± 0.01	13.5 ± 0.6	0.13 ± 0.01	67 ± 8
	1−16	0.05 ± 0.01	2.4 ± 0.1	0.24 ± 0.01	11.4 ± 0.1	0.07 ± 0.01	54 ± 2
	1−20	0.04 ± 0.01	1.9 ± 0.4	0.25 ± 0.01	8.6 ± 0.8	0.06 ± 0.01	39 ± 5
	1−30	0.04 ± 0.01	1.6 ± 0.3	0.23 ± 0.01	5.9 ± 0.2	0.08 ± 0.01	16 ± 2
	1−40	0.04 ± 0.01	1.8 ± 0.4	0.24 ± 0.02	5.4 ± 0.3	0.07 ± 0.03	14 ± 3
	1−100	0.02 ± 0.01	1.4[b]	0.23 ± 0.05	4.0 ± 0.6	0.10 ± 0.06	8.3 ± 1.4
	D_2O[35]	0.073 ± 0.002	1.4 ± 0.1	0.304 ± 0.003	4.5 ± 0.1		
Mg^{2+}	1−12	0.064 ± 0.007	15 ± 3	0.316 ± 0.008	226 ± 27		
	1−16	0.06 ± 0.02	8 ± 2	0.31 ± 0.02	148 ± 17		
	1−20	0.083 ± 0.002	7.4 ± 0.9	0.290 ± 0.006	119 ± 9		
	1−30	0.08 ± 0.02	3.4 ± 0.4	0.31 ± 0.03	83 ± 4		
	1−40	0.08 ± 0.02	3 ± 1	0.31 ± 0.03	78 ± 7		
	1−100	0.17 ± 0.02	2.9 ± 0.1	0.23 ± 0.02	59 ± 8		

[a]Multiexponential fit parameters to the anisotropy for $SeCN^-$ associated with D_2O (top half of table) in aqueous solutions with varying concentrations of $MgCl_2$. For the anisotropy decays measured for $SeCN^-$ associated with Mg^{2+} (bottom half) in the same solutions, the parameters are extracted from a two-component fit. The A_i and t_i are the amplitude and time constant of the i^{th} component. [b]This value was fixed in the fitting.

anisotropy decays accurately. Figure 3b shows the two-component fits to the Mg^{2+} anisotropy data at the center frequency, which includes contributions from the D_2O anisotropy. Table 2 gives the anisotropy parameters for both D_2O and Mg^{2+}. Note that at all concentrations, the slowest Mg^{2+} component t_2 is much slower than the slowest D_2O component t_3. Thus, the Mg^{2+} t_2 obtained from the two component fits is essentially the same as the t_2 determined from a preliminary biexponential fit to the Mg^{2+} data before accounting for the D_2O contribution (see t_2 in Table S2 in the SI). Only the Mg^{2+} t_1 is altered by the D_2O contribution (primarily for the lower Mg^{2+} concentrations), and it can be determined from the two-component fits shown in Figure 3b.

Like the time scales of the D_2O dynamics, the time scales of the Mg^{2+} dynamics increase monotonically with increasing salt concentration, from 2.9 and 59 ps for 1−100 to 15 and 226 ps for 1−12. The relative amplitudes also remain roughly constant (~20% for t_1 and ~80% for t_2). The only exception is the 1−100 concentration, which has more weight in the first time constant. Slower Mg^{2+} bound (vs D_2O bound) dynamics of another anionic nitrile probe (SCN^-) in aqueous MgI_2[31,32] and $Mg(ClO_4)_2$[30] solutions were also observed.

The multiexponential $r(t)$ decays can be understood in terms of the wobbling-in-a-cone model of restricted orientational diffusion.[45−48] The orientational correlation function $C_2(t)$ is modeled with ultrafast inertial motions, diffusive time constant(s) for restricted angular diffusion ("wobbling" motions), and a final time constant τ_m for complete orientational randomization.[61] The inertial and wobbling motions have associated half angles θ quantifying the angular cones explored by the CN transition dipole in the corresponding restricted reorientation processes. As the solvent structure evolves, constraints on angular displacement are relaxed and the CN dipole explores increasingly greater angular space. Detailed description of these parameters (tabulated in Table S3) and the model are given in the SI along with the relevant equations (eqs S2 and S3).

The inertial cone angle θ_{in} is ~16−17° for the D_2O peak and is <12° for the Mg^{2+} peak. In a study of an ionic liquid (IL), two different selenocyanate probes were used, one as the free anion $SeCN^-$ with θ_{in} = 15.2° and one covalently incorporated into the cation of the IL as 2-SeCN-$Bmim^+$ (Bmim being 1-butyl-3-methylimidazolium), with θ_{in} = 10°.[40] The 15.2° and 10° cone angles are strikingly similar to the D_2O- and Mg^{2+}-associated θ_{in} of 16° and 12°, respectively, at the higher concentration $MgCl_2$ solutions. In the IL study, the trend extends, with smaller wobbling cone angles and longer time scales for the positively charged 2-SeCN-$Bmim^+$. While the wobbling cone angles for the D_2O- and Mg^{2+}-associated species cannot be directly compared, as there are two for D_2O and one for Mg^{2+}, the total cone angle θ_{tot} follows the same trend of being smaller for the Mg^{2+} species (22° vs 48°, for 1−12 mole ratio). As explored in Section III.D, the $SeCN^-$ associated with Mg^{2+} is likely one member of the Mg^{2+} first coordination shell, and the complex bears a positive charge like the 2-SeCN-$Bmim^+$. The fact that the cone angles are smaller for Mg^{2+}-associated $SeCN^-$ suggests that this $SeCN^-$ species must have a structure analogous to the 2-SeCN-$Bmim^+$ that imposes greater angular restriction on the CN via steric hindrance and interactions. This provides further evidence for the $SeCN^-$ being strongly bound to the four- to six-coordinated Mg^{2+} structure, in contrast to the "free" $SeCN^-$ that is associated with a D_2O.

III.D. Hydrodynamic Theory and the SED Model. The wobbling-in-a-cone model offers information about the restricted reorientation processes. Hydrodynamic theory can provide insights on the complete unrestricted orientational relaxation. The theory proposes that the complete reorientation time τ_m is proportional to the bulk dynamic viscosity η of the solvent and the volume V of the rotator (e.g, the vibrational probe), and inversely proportional to the absolute temperature T:[68−70]

$$\tau_m = \frac{\eta V}{k_B T} \tag{3}$$

Equation 3 is the Stokes−Einstein−Debye (SED) equation, which applies to a spherical rotator with stick boundary conditions, where the rotator has volume $V = \frac{4}{3}\pi r^3$ and k_B is the Boltzmann constant. Modifications can be used to extend the model: $\tau_m = (\eta/T)^x \times (V/k_B) \times fC$. In the SED model, the exponent x = 1 and the correction factors f (shape or Perrin factor) and C (interaction or boundary condition factor) are both unity,[71,72] which gives eq 3.

In Figure 4a, the logarithm of τ_m is plotted against the logarithm of η/T. The viscosities of the $MgCl_2$ solution

https://doi.org/10.1021/acs.jpcb.3c00300
J. Phys. Chem. B 2023, 127, 3278−3290

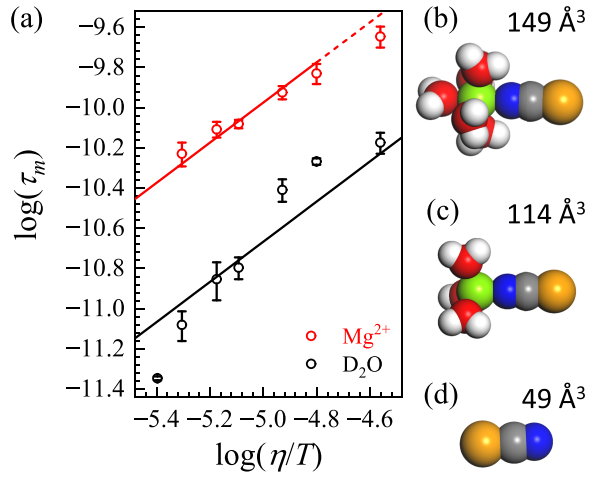

Figure 4. (a) Log−log plots of the orientational relaxation time τ_m (in seconds) versus the ratio η/T of the viscosity (in Pa·s) to the temperature (fixed at ∼295 K). The lines are all fits with fixed unity slope, in accordance to the standard SED model (see text). For the Mg^{2+} peak, the fit is to the lower concentrations (1−100 to 1−16), which extends (dashed line) above the highest concentration data point (1−12). For comparison to the volumes extracted from the log−log plots, the volumes of the $SeCN^-$ probe in various optimized structures were calculated: (b) $[Mg(H_2O)_5(SeCN)]^+$, (c) $[Mg(H_2O)_3(SeCN)]^+$, and (d) $SeCN^-$.

increase with concentration (Table S1), so the less negative values on the x-axis correspond to higher concentrations and viscosities. The less negative values on the y-axis correspond to longer τ_m. This representation of the data corresponds to taking the logarithm of eq 3, yielding a linear equation:

$$\log(\tau_m) = \log\left(\frac{\eta}{T}\right) + \log\left(\frac{V}{k_B}\right) \quad (4)$$

The $\log(\eta/T)$ term is the independent variable and has a coefficient of 1, corresponding to $x = 1$, and the $\log(V/k_B)$ term is the intercept. Non-unity values of x are possible for liquids exhibiting fractional SED behavior and are related to solute size and intermolecular interactions.[73−75] The slope of the linear fit in the log−log plot offers a way to examine the linearity (i.e., $x = 1$) of the relationship between τ_m and η (T is constant). The fits shown in Figure 4a have slopes fixed to unity. If the correction factors $f = 1$ and $C = 1$ are included, they would give a constant term, $\log(fC) = 0$, which alters the intercept when nonzero, giving a different volume V.

Depending on concentration, τ_m for Mg^{2+} (t_2, Table 2) is between three to eight times greater than for D_2O (t_3, Table 2). This difference can arise from different boundary conditions and non-spherical shape of the rotator (i.e., the $\log(fC)$ term), but a simpler explanation is a difference in their hydrodynamic volumes (i.e., the $\log(V/k_B)$ term), with the $SeCN^-$ bound to Mg^{2+} with its solvation shell having a larger hydrodynamic volume and slower reorientation.

In Figure 4a, the solid red line is the fit to the lower five concentrations, and the dashed line an extension of the fit to the highest concentration. The deviation from a linear trend for the 1−12 concentration was previously seen for the FWHM (Section III.A). Figure 4b,c shows two proposed structures of the Mg^{2+} bound $SeCN^-$ complexes, along with their corresponding volumes: a six-coordinated Mg^{2+} (149 Å^3) and a four-coordinated Mg^{2+} (114 Å^3), with five and three waters, respectively. A free $SeCN^-$ ion (Figure 4d) has a volume of 49 Å^3. These are van der Waals volumes of structures optimized using Gaussian 16 with a B3LYP/6-311 + G(d, p) basis set. The 49 Å^3 volume of $SeCN^-$ is in good agreement with previous modeling of $SeCN^-$ as a prolate spheroid with ∼40−65 Å^3 volume.[76] The Mg−O distance of 2.1 Å in hydration structures optimized without the $SeCN^-$ are in good agreement with X-ray diffraction studies,[21−23] and this distance does not change significantly in heavy water,[24] suggesting that the structures used for the volume calculations should be reasonable representations of the solutions being studied. The 147 Å^3 volume extracted from the solid red line (concentrations 1−100 to 1−16) is very different from the 49 Å^3 volume of a free $SeCN^-$ (Figure 4d) and is almost exactly the same as the 149 Å^3 volume of the six-coordinated Mg^{2+} structure (Figure 4b). This indicates that the Mg^{2+} bound $SeCN^-$ moves as a unit with the rest of the Mg^{2+} hydration structure. A volume of 114 Å^3 can be calculated using eq 3 from the τ_m and η of the 1−12 concentration, which is exactly the volume of the four-coordinated Mg^{2+} structure (Figure 4c). This provides further evidence that the Mg^{2+} hydration number decreases from six to four as fewer water molecules are available to solvate the cation at the highest concentration.

The fit to the D_2O data (black line, Figure 4a) roughly goes through the data points and gives a volume of 30 Å^3. This is not too far removed from the 49 Å^3 volume calculated for $SeCN^-$ (Figure 4d). The deviation of the data from the SED fit may be a result of the nonspherical shape of $SeCN^-$ and departure from Debye diffusion behavior (see SI).

Independent of the details of the fits, the significant difference in τ_m of the D_2O- and Mg^{2+}-associated $SeCN^-$ species supports the idea of two very different-sized rotators. The volumes extracted from the τ_m support the picture of the D_2O-associated $SeCN^-$ rotating freely as an anion and the Mg^{2+}-associated $SeCN^-$ rotating as part of a larger unit involving the first solvation shell of Mg^{2+}, which changes coordination at a sufficiently high concentration. Compared to X-ray diffraction or isotopic dilution studies that give specific information about the first coordination shell of a cation, the transport properties of ions typically give a wide range of solvation numbers, depending on whether or not secondary shell molecules (waters or even counterions) are also dragged along.[77] Thus, observation of the subtle change from an octahedral to a tetrahedral solvation sphere here is particularly interesting. The tight binding of both the $SeCN^-$ probe and the solvating water molecules to the Mg^{2+} and the relatively slow water exchange in the Mg^{2+} first solvation shell enabled the six- or four-coordinated shell to rotate as a distinct unit on the time scales of the experiment.

III.E. Spectral Diffusion. *III.E.1. CLS and FFCF.* The 2D spectra for three concentrations (1−12, 1−20, and 1−100) are shown at T_w = 1.5 and 30 ps in Figure 5. There are two 0−1 transitions (red, positive going peaks): the lower frequency D_2O-associated peak (ω_1 ∼2075 cm^{-1}) and the higher frequency Mg^{2+}-associated peak (ω_1 ∼2115 cm^{-1}). The two 1−2 transitions (blue, negative going peaks) have the same ω_1 frequency as the corresponding 0−1 peaks but are shifted to lower frequencies along ω_3 by the vibrational anharmonicity. As previously mentioned and seen in the 2D spectra, the D_2O and Mg^{2+} bands overlap with each other. The experimental D_2O (or Mg^{2+}) 0−1 transition was isolated (Figure S5) by subtracting the three other peaks, which were modeled by 2D Gaussian functions in a global fit of all peaks (Figure S4). This

https://doi.org/10.1021/acs.jpcb.3c00300
J. Phys. Chem. B 2023, 127, 3278−3290

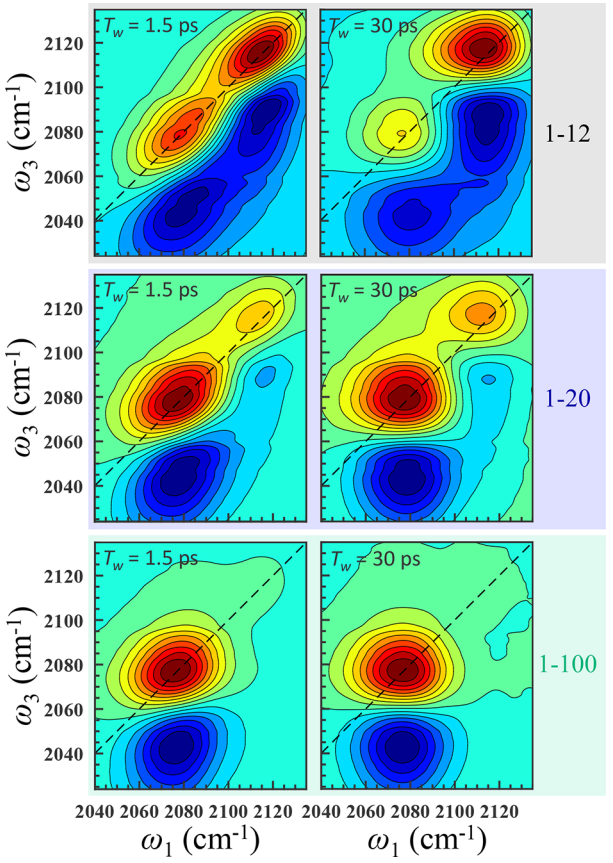

Figure 5. 2D IR spectra of the CN stretch of $SeCN^-$ in D_2O solutions of varying $MgCl_2$ concentrations at time delays T_w = 1.5 and 30 ps.

fitting and subtraction process is described in the SI and detailed in a previous publication.[33] All 2D spectra shown are isotropic (i.e., constructed from parallel and perpendicular polarization 2D spectra) and reflect the structural spectral diffusion dynamics. The reorientation-induced spectral diffusion[78−80] contributions to the spectral diffusion are minor for both peaks and will not be considered (see SI). The 1−12 concentration dynamics for the D_2O peak and the 1−100 dynamics for the Mg^{2+} peak could not be reliably determined due to their small signals and associated complications from the peak separation.

When two distinct populations of the vibrational probe are in equilibrium in solution, the switching of the bonding partner, i.e., chemical exchange, on time scales shorter than or comparable to the dynamics distorts the measurements and results in off-diagonal peaks in the 2D spectra.[30−33,81] We do not observe chemical exchange of $SeCN^-$ in aqueous $MgCl_2$ solutions on the time scales of our measurements. This can be seen by inspection of the 30 ps spectra in Figure 5. Chemical exchange would give rise to off-diagonal peaks growing in with T_w. These 0−1 (red, positive going) peaks would be located at (ω_1, ω_3) = (2075 cm^{-1}, 2115 cm^{-1}) and (2115 cm^{-1}, 2075 cm^{-1}). The first of these would be more prominent as the second peak would overlap with the negative going 1−2 Mg^{2+} peak. There is no evidence of off-diagonal peaks. The lack of chemical exchange on the experimental time scale is consistent with other experiments. Water-anion exchange (exchange of D_2O and $SeCN^-$ in the first solvation shell of Mg^{2+}) should not be observed due to the long, microsecond scale water residence time.[20,44] Anion exchange (exchange of $SeCN^-$ and Cl^- in the first solvation shell of Mg^{2+}) has not been observed for similar experiments with SCN^- in aqueous $MgCl_2$ solution, but has been observed in MgI_2 and $MgBr_2$ solutions.[31] This is due to the lack of $MgCl_2$ contact ion pairing in aqueous $MgCl_2$ solutions, even at high concentrations.[20,49,82]

As seen in the left column of Figure 5, the shapes of the 0−1 transitions at short time (T_w = 1.5 ps) are elongated along the diagonal, indicating strong correlation between the initial (ω_1) and final (ω_3) frequencies (i.e., $\omega_1 \approx \omega_3$). At later time T_w = 30 ps (right column of Figure 5), as the liquid structure has evolved over the T_w period, there is a loss of correlation between ω_1 and ω_3, resulting in rounder peaks. The loss of correlation was quantified with the center line slope (CLS) method.[83−85] The CLS is the normalized frequency−frequency correlation function (FFCF), the probability that a vibrational probe with a given initial frequency has the same frequency at T_w, averaged over all frequencies ω in the absorption band.[57,83−85] CLS values are extracted at each T_w from a series of 2D spectra collected at different T_w's to form a decay curve (Figure 6). Biexponential (D_2O) and triexponential (Mg^{2+}) fits to the CLS decays are shown in Figure 6 as solid lines and the fitting parameters are tabulated in Table S4.

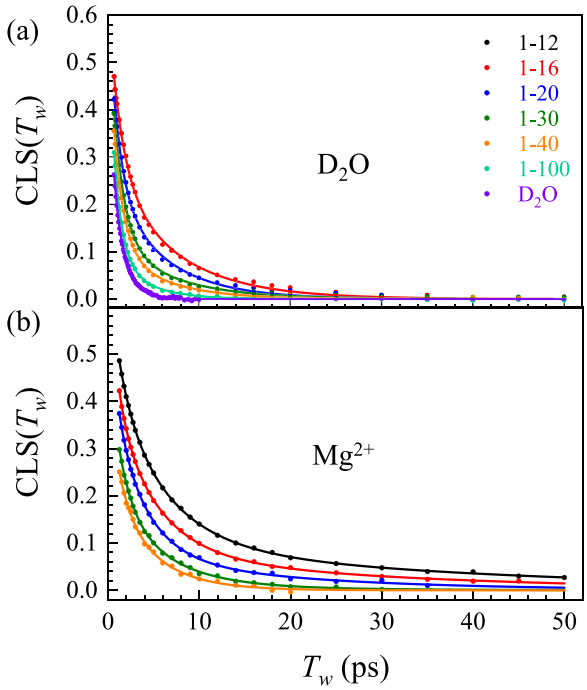

Figure 6. Measured CLS(T_w) decays (spectral diffusion) of the CN stretch of $SeCN^-$ in D_2O solutions of varying $MgCl_2$ concentrations and in pure D_2O. The CLS is the normalized frequency−frequency correlation function. (a) The solid curves are biexponential fits to the data for the D_2O peak. (b) The solid curves are multiexponential fits to the data for the Mg^{2+} peak.

The FFCF was determined from the CLS and the linear absorption spectrum using CAFE, a program that employs artificial neural networks to rapidly calculate the FFCF parameters (Table 3).[85] The complete FFCF is commonly described by the Kubo model:[57,86]

$$\mathrm{FFCF} = \langle \delta\omega(T_w)\delta\omega(0)\rangle = \frac{\delta(T_w)}{T_2} + \sum_i \Delta_i^2 \exp(-T_w/t_i) \quad (5)$$

https://doi.org/10.1021/acs.jpcb.3c00300
J. Phys. Chem. B 2023, 127, 3278−3290

Table 3. FFCF Parameters[a]

sample		T_2 (ps)	Γ (cm^{-1})	Δ_1 (cm^{-1})	t_1 (ps)	Δ_2 (cm^{-1})	t_2 (ps)	Δ_3 (cm^{-1})	t_3 (ps)
D_2O	1−12								
	1−16	1.2 ± 0.3	9 ± 3	13.3 ± 0.5	1.4 ± 0.2	8.7 ± 0.8	8 ± 1		
	1−20	1.6 ± 0.5	7 ± 2	13.7 ± 0.2	1.1 ± 0.1	8.1 ± 0.7	6 ± 1		
	1−30	1.6 ± 0.8	8 ± 3	13.9 ± 0.7	1.2 ± 0.1	5.7 ± 0.5	7 ± 1		
	1−40	1.3 ± 0.2	8 ± 1	13.6 ± 0.5	1.1 ± 0.1	5.1 ± 0.2	6 ± 1		
	1−100	1.8 ± 0.8	7 ± 4	14 ± 1	0.9 ± 0.2	5.0 ± 0.7	3 ± 1		
	D_2O[35]	1.4 ± 0.1	7.6 ± 0.2	9.7 ± 0.5	0.6 ± 0.1	10.2 ± 0.8	1.4 ± 0.2		
Mg^{2+}	1−12	2.2 ± 0.6	5 ± 1	6.7 ± 0.4	1.5 ± 0.1	7.2 ± 0.2	5.4 ± 0.2	3.8 ± 0.4	34 ± 1
	1−16	2.6 ± 0.5	4 ± 1	7.3 ± 0.3	1.2 ± 0.2	6.5 ± 0.2	4.8 ± 0.5	3.1 ± 0.3	29 ± 4
	1−20	2.1 ± 0.4	5 ± 1	6.6 ± 0.2	1.3 ± 0.3	6.0 ± 0.3	3.9 ± 0.2	2.4 ± 0.5	21 ± 5
	1−30	1.9 ± 0.4	6 ± 1	5.9 ± 0.4	1.2 ± 0.3	4.3 ± 0.3	4.0 ± 0.2	1.7 ± 0.2	13 ± 3
	1−40	1.7 ± 0.1	6.3 ± 0.4	4.6 ± 0.2	1.5 ± 0.3	3.3 ± 0.4	4.8 ± 0.5		
	1−100								

[a] T_2: observed homogeneous dephasing time; $\Gamma = 1/\pi T_2$: homogeneous line width; Δ_i and t_i: frequency fluctuation amplitude and time constant for the i^{th} component, respectively.

where the frequency fluctuation $\delta\omega(T_w)$ is the difference between the instantaneous frequency $\omega(T_w)$ and the average frequency $\langle\omega\rangle$, $\delta(T_w)$ is the Dirac delta function, T_2 is the total homogeneous dephasing time, and Δ_i and t_i are the amplitude of the frequency fluctuation and time constant of the i^{th} decay, respectively. The time constants t_i of the FFCF are the same as those extracted from the CLS fits. In contrast to the normalized amplitudes of the CLS, the frequency fluctuation amplitudes Δ_i in the FFCF are in absolute frequency units (cm^{-1}).

The FFCF components can be separated into homogeneous and inhomogeneous contributions. A component is considered motionally narrowed (homogeneous) if $\Delta_i t_i < 1$ (Δ_i in angular frequency units) and inhomogeneously broadened otherwise.[57] In the former case, Δ and t cannot be independently determined. The motionally narrowed contribution to the absorption spectrum has a pure dephasing linewidth $\Gamma^* = \Delta^2 t/\pi = 1/\pi T_2^*$, where T_2^* is the pure dephasing time. The observed total homogeneous (Lorentzian) linewidth is $\Gamma = 1/\pi T_2$, and the dephasing time T_2 has contributions from the vibrational lifetime T_1 and the orientational relaxation time T_{or}:[83]

$$\frac{1}{T_2} = \frac{1}{T_2^*} + \frac{1}{2T_1} + \frac{1}{3T_{or}} \tag{6}$$

The total homogeneous linewidth Γ is ∼8 cm^{-1} for the D_2O peak and ∼ 5 cm^{-1} for the Mg^{2+} peak across all concentrations (Table 3). Both are dominated by motionally narrowed pure dephasing, as the lifetime and orientational relaxation contributions combined make up <1 cm^{-1} (∼0.2 cm^{-1} for Mg^{2+}). The total inhomogeneous linewidth is the convolution of the Gaussian components with standard deviations Δ_i given by FWHM $= 2(2\ln 2)^{1/2}\Delta_{total}$, where $\Delta_{total} = (\sum_i \Delta_i^2)^{1/2}$. The total linear absorption line shape depends on both the Δ_i's and the t_i's and can be determined from the FFCF.[85]

In general, the value of the CLS at $T_w = 0$ starts below one (with one being perfect correlation) (Figure 6) due to the T_w-independent homogeneous broadening. The higher the initial CLS value, the lower the contribution of the homogeneous broadening to the spectral linewidth. Since the homogeneous linewidth Γ is essentially constant within experimental error across concentrations for both peaks (Table 3) and the relative contribution of the homogeneous broadening decreases with increasing concentration (Figure 6), the overall spectral broadening (FWHM) is primarily due to inhomogeneous broadening, as discussed in Section III.A.

The first spectral diffusion times (Table 3) are basically the same for the two peaks. For all salt concentrations, both peaks are in the range of ∼1−1.5 ps with the error bars almost overlapping for both species. In pure D_2O, the value is 0.6 ps.[35] This fast time constant is frequently associated with very local H-bond fluctuations, primarily in bond length.[33,35,61,87,88] The second time scale is ∼4−5 ps for the Mg^{2+} peak. The D_2O peak t_2 increases from 1.4 ps in pure D_2O to 3 ps in the 1−100 solution and then remains at ∼6−8 ps at the higher concentrations. In pure D_2O, the second time scale was attributed to the complete randomization of the H-bond network.[35,88] For the D_2O peak, the contribution (from Δ_1) of the first component is ∼13 cm^{-1} across concentrations, whereas the second component increases from 5.0 to 8.7 cm^{-1} with increasing concentration, suggesting that the dynamical slowing (Figure 6a) with concentration derives from spectral broadening associated with structural changes in the H-bond network and slowing of the H-bond network randomization. The jump in t_2 from ∼3 ps at 1−100 to 6−8 ps at 1−40 and higher concentrations may be a result of the number of well solvated ions decaying to zero at concentrations close to 1−40,[49] as the number of waters adjacent to other waters decreases and the number adjacent to ions increases. These new solvent structures increase the linewidth and slow down the H-bond network randomization.

III.E.2. Long Time Spectral Diffusion. For the Mg^{2+} peak, there is a third time component of the FFCF, which increases from 13 ps in the 1−30 solution to 34 ps in the 1−12 solution. The Δ's and t's of the latter two components both increase with increasing concentration. The slowing of the Mg^{2+} spectral diffusion thus stems from both increases in inhomogeneous broadening and the slowing of each process. The observation of a third time scale only for the Mg^{2+} peak parallels the spectral diffusion dynamics in the IL discussed in previous sections, in which biexponential and triexponential dynamics were observed for the two different probes, the negatively charged $SeCN^-$ and the positively charged 2-SeCN-$Bmim^+$, respectively.[40] In both the IL and in $MgCl_2$ solution, the selenocyanate moiety in the bulkier positively charged structure displayed slower dynamics and a third time constant. In the IL, small vibrational probes like $SeCN^-$,[40,76] water, methanol,[61] and CO_2[78] sample their entire inhomogeneous

https://doi.org/10.1021/acs.jpcb.3c00300
J. Phys. Chem. B 2023, 127, 3278−3290

lines before total randomization of the liquid structure. The inhomogeneous line of a particular probe reflects only those liquid structures that affect the probe frequency. These IL results indicate that the intermolecular interactions that give rise to the free $SeCN^-$ inhomogeneous linewidth and the corresponding dynamics that sample them do not involve all structural degrees of freedom of the liquid. Complete randomization of a liquid's structure can be measured using optically heterodyne-detected optical Kerr effect (OHD-OKE) spectroscopy.[40] Using $SeCN^-$ in the IL, the longest time scale obtained, 94 ps, is almost an order of magnitude faster than the complete structural randomization time, 870 ps, measured by OKE. The additional time scale probed by 2-SeCN-$Bmim^+$, 600 ps, is close to the time scale given by OKE. It should be noted that the two experiments measure different correlation functions, the FFCF for the 2D IR and the polarizability-polarizability correlation function for OKE. These two correlations functions would not be expected to report identical time constants.

OKE measurements performed in a manner previously described[89] in aqueous LiCl solutions (there are no experimental measurements for $MgCl_2$ yet) show that the complete structural randomization time increases with increasing salt concentration to ~25 ps. This time is on the same order of magnitude as the t_3's (13−34 ps) measured in this study for the Mg^{2+} peak. Although we do not expect OKE time constants to be identical to those of the FFCF, a longer time constant in $MgCl_2$ (i.e., 34 ps at higher concentrations vs 25 ps for LiCl) may be expected due to the larger cation charge. A simulation study of OKE signals in aqueous NaCl, $MgCl_2$, and $AlCl_3$ solutions shows that the OKE signal decays more slowly with increasing cation charge, primarily due to the slower motions of first hydration shell waters that are strongly coordinated to the cation.[90,91]

We observe a saturation effect in the trend of the third time scale for the Mg^{2+} peak, as the Δ_3 component is not present for the lowest measurable concentration (1−40), becomes present at 1−30, and both Δ_3 and t_3 increase with concentration and begin to plateau between 1−16 and 1−12. The leveling off between the two highest concentrations was also observed for the FWHM and hydrodynamic behavior discussed in previous sections.

It is interesting to note that the spectral diffusion time scales for both D_2O and Mg^{2+} peaks are much shorter than the complete reorientation time scales, showing that the different correlation functions are sensitive to different underlying physical motions. What is similar for the two dynamical observables is that the two populations of $SeCN^-$ report on distinct dynamics, illustrating the heterogeneity in liquid structure and the impact that the divalent Mg^{2+} has on $MgCl_2$ solution over a range of concentrations. A previous work has shown $SeCN^-$ to be a reliable probe of local H-bond fluctuations and the global H-bond network rearrangements in water,[35] and in $MgCl_2$, the $SeCN^-$ associated with D_2O has biexponential spectral diffusion dynamics analogous to those in pure D_2O. The association of the $SeCN^-$ probe with Mg^{2+} gives rise to distinct spectral diffusion dynamics with an additional time scale that is suggestive of the effects of a tightly held first hydration layer.

IV. CONCLUDING REMARKS

The dynamics and structures reported by the $SeCN^-$ vibrational probes associated with D_2O and with the Mg^{2+} cation differed as shown by the IR observables studied here for aqueous $MgCl_2$ solutions, ranging from relatively dilute to near saturated concentrations. The two species are spectrally distinct (Figure 1) and do not undergo chemical exchange, allowing for robust separation and analysis of their respective line shapes and dynamics, as measured by FT-IR, polarization selective pump-probe spectroscopy, and 2D IR vibrational echo experiments.

Both the D_2O- and Mg^{2+}-associated line shapes broaden with increasing salt concentration (Table 1), sampling an increasing variety of solvent configurations as the populations of free ions fall and the solvent-shared ion pairs rise.[49] For the Mg^{2+} band FWHM, saturation effects begin at a concentration between 1−16 and 1−12 mole ratios (Figure 2). This is also the case for the complete reorientation time (Figure 4). The hydrodynamic volume of the $SeCN^-$ incorporated into the hydrated Mg^{2+} complex changes in a manner consistent with the complex going from a six- to four-coordinated structure as the number of waters available for coordination decreases with increasing salt concentration. For the D_2O peak, the rotational and spectral diffusion dynamics at lower concentrations are similar to those in pure D_2O and slow with increasing salt concentrations.

The disparate behaviors of the free $SeCN^-$ (D_2O peak) and $SeCN^-$ incorporated into the Mg^{2+} coordination sphere (Mg^{2+} peak) in $MgCl_2$ solution are similar to those of a $SeCN^-$ anion and a selenocyanate covalently incorporated into an imidazolium cation in an imidazolium ionic liquid.[40] The probe molecules undergo orientational relaxation over multiple time scales with successive angular constraint release, modeled by wobbling and free diffusion processes. Like the imidazolium cation-bound selenocyanate, the $SeCN^-$ coordinated to the hydrated Mg^{2+} cation is sterically hindered and thus has smaller cone angles (Table S3) than the free $SeCN^-$ species. The Mg^{2+} complex also has slower complete reorientation times (Table 2) that agree with hydrodynamic theory given the predicted volume of its coordination structure (vs free $SeCN^-$) and the solution viscosities. It also displays a third spectral diffusion time scale that is almost an order of magnitude longer than that of the D_2O-associated $SeCN^-$ (Table 3).

The distinct dynamics sensed by $SeCN^-$ in $MgCl_2$ reveal differences in the underlying solvation structures. The different spectral characteristics and dynamics reported by the $SeCN^-$ N lone pair bound to a water versus bound to the charge dense Mg^{2+} cation are caused by three features attributed to $MgCl_2$ solutions over a wide range of concentrations: slow water exchange in the Mg^{2+} solvent shell, lack of Mg^{2+}-Cl^- contact ion pairing, and a Mg^{2+} coordination number of six (four at saturated concentrations).

■ ASSOCIATED CONTENT

Data Availability Statement

Data are available by contacting Professor Michael D. Fayer, Department of Chemistry, Stanford University, Stanford, CA 94305−5080. Email: fayer@stanford.edu.

Supporting Information

The Supporting Information is available free of charge at https://pubs.acs.org/doi/10.1021/acs.jpcb.3c00300.

Additional sample preparation details, solution properties, isotropic pump-probe signals, two-component fits, wobbling-in-a-cone analysis, deviations from SED

https://doi.org/10.1021/acs.jpcb.3c00300
J. Phys. Chem. B 2023, 127, 3278−3290

behavior, 2D Gaussian subtraction, decays in different polarization configurations, and CLS parameters (PDF)

AUTHOR INFORMATION

Corresponding Author

Michael D. Fayer − *Department of Chemistry, Stanford University, Stanford, California 94305, United States;* orcid.org/0000-0002-0021-1815; Phone: (650) 723-4446; Email: fayer@stanford.edu

Authors

Samantha T. Hung − *Department of Chemistry, Stanford University, Stanford, California 94305, United States;* orcid.org/0000-0001-9448-0962

Sean A. Roget − *Department of Chemistry, Stanford University, Stanford, California 94305, United States;* orcid.org/0000-0003-2470-3571

Weizhong Zheng − *State Key Laboratory of Chemical Engineering, East China University of Science and Technology, Shanghai 200237, China*

Complete contact information is available at: https://pubs.acs.org/10.1021/acs.jpcb.3c00300

Notes

The authors declare no competing financial interest.

ACKNOWLEDGMENTS

We would like to thank Prof. Ward Thompson for many helpful discussions. We also thank Stephen Van Wyck for his OKE measurements in aqueous lithium chloride solutions. This work was supported by the National Science Foundation, Division of Chemistry, Award Number 1954392. S.T.H. acknowledges partial support from an ARCS fellowship.

REFERENCES

(1) Mirchamsy, H.; Shafyi, A.; Mahinpour, M.; Nazari, P. Stabilizing Effect of Magnesium Chloride and Sucrose on Sabin Live Polio Vaccine. *Dev. Biol. Stand.* **1978**, *41*, 255−257.

(2) Chen, C.-H.; Wu, R.; Roth, L. G.; Guillot, S.; Crainic, R. Elucidating Mechanisms of Thermostabilization of Poliovirus by D_2O and $MgCl_2$. *Arch. Biochem. Biophys.* **1997**, *342*, 108−116.

(3) Kumru, O. S.; Joshi, S. B.; Smith, D. E.; Middaugh, C. R.; Prusik, T.; Volkin, D. B. Vaccine Instability in the Cold Chain: Mechanisms, Analysis and Formulation Strategies. *Biologicals* **2014**, *42*, 237−259.

(4) Peng, B.; Chen, J. Functional Materials with High-Efficiency Energy Storage and Conversion for Batteries and Fuel Cells. *Coord. Chem. Rev.* **2009**, *253*, 2805−2813.

(5) Wang, F.; Fan, X.; Gao, T.; Sun, W.; Ma, Z.; Yang, C.; Han, F.; Xu, K.; Wang, C. High-Voltage Aqueous Magnesium Ion Batteries. *ACS Cent. Sci.* **2017**, *3*, 1121−1128.

(6) Huang, J.; Dong, X.; Guo, Z.; Wang, Y. Progress of Organic Electrodes in Aqueous Electrolyte for Energy Storage and Conversion. *Angew. Chem.* **2020**, *132*, 18478−18489.

(7) Wang, Q.; Luan, Z.; Wei, N.; Li, J.; Liu, C. The Color Removal of Dye Wastewater by Magnesium Chloride/Red Mud (MRM) from Aqueous Solution. *J. Hazard. Mater.* **2009**, *170*, 690−698.

(8) Daloee, T. S.; Behbahani, F. K. $MgCl_2$ and Its Applications in Organic Chemistry and Biochemistry: A Review. *Mol. Diversity* **2020**, *24*, 463−476.

(9) Garfinkel, L.; Garfinkel, D. Magnesium Regulation of the Glycolytic Pathway and the Enzymes Involved. *Magnesium* **1985**, *4*, 60−72.

(10) Theophanides, T.; Angiboust, J.; Polissiou, M.; Anastassopoulou, J.; Manfait, M. Possible Role of Water Structure in Biological Magnesium Systems. *Magnesium Res.* **1990**, *3*, 5−13.

(11) *CRC Handbook of Chemistry and Physics*; 77th ed.; CRC Press: Boca Rotan, FL, 1996.

(12) Rubenowitz, E.; Axelsson, G.; Rylander, R. Magnesium and Calcium in Drinking Water and Death from Acute Myocardial Infarction in Women. *Epidemiology* **1999**, 31−36.

(13) Choi, M. Y.; Chan, C. K. Continuous Measurements of the Water Activities of the Mg^{2+}− Ca^{2+}− Na^{+}− Cl^{-}− NO_3^{-}− SO_4^{2-}− H_2O System. *J. Chem. Eng. Data* **2002**, *47*, 1526−1531.

(14) Cowan, J. Structural and Catalytic Chemistry of Magnesium-Dependent Enzymes. *BioMetals* **2002**, *15*, 225−235.

(15) Gibson, E. R.; Hudson, P. K.; Grassian, V. H. Physicochemical Properties of Nitrate Aerosols: Implications for the Atmosphere. *J. Phys. Chem. A* **2006**, *110*, 11785−11799.

(16) Guéroult, M.; Boittin, O.; Mauffret, O.; Etchebest, C.; Hartmann, B. Mg^{2+} in the Major Groove Modulates B-DNA Structure and Dynamics. *PLoS One* **2012**, *7*, No. e41704.

(17) Ignatov, I.; Mosin, O. Research of Mountain and Melt Water as Factors of Longevity. Effects of Calcium, Magnesium, Zinc and Manganese. *J. Med. Physiol. Biophys.* **2015**, *15*, 42−60.

(18) Friesen, S.; Hefter, G.; Buchner, R. Cation Hydration and Ion Pairing in Aqueous Solutions of $MgCl_2$ and $CaCl_2$. *J. Phys. Chem. B* **2019**, *123*, 891−900.

(19) Bruni, F.; Imberti, S.; Mancinelli, R.; Ricci, M. A. Aqueous Solutions of Divalent Chlorides: Ions Hydration Shell and Water Structure. *J. Chem. Phys.* **2012**, *136*, No. 064520.

(20) Callahan, K. M.; Casillas-Ituarte, N. N.; Roeselová, M.; Allen, H. C.; Tobias, D. J. Solvation of Magnesium Dication: Molecular Dynamics Simulation and Vibrational Spectroscopic Study of Magnesium Chloride in Aqueous Solutions. *J. Phys. Chem. A* **2010**, *114*, 5141−5148.

(21) Dorosh, A. K.; Skryshevskii, A. F. The Structural Characteristics of the Immediate Environment of Cations in Aqueous Solutions. *J. Struct. Chem.* **1965**, *5*, 842−844.

(22) Albright, J. N. X-Ray Diffraction Studies of Aqueous Alkaline-Earth Chloride Solutions. *J. Chem. Phys.* **1972**, *56*, 3783−3786.

(23) Caminiti, R.; Licheri, G.; Piccaluga, G.; Pinna, G. X-Ray Diffraction Study of $MgCl_2$ Aqueous Solutions. *J. Appl. Crystallogr.* **1979**, *12*, 34−38.

(24) Skipper, N. T.; Neilson, G. W.; Cummings, S. C. An X-Ray Diffraction Study of $Ni_{(Aq)}^{2+}$ and $Mg_{(Aq)}^{2+}$ by Difference Methods. *J. Phys.: Condens. Matter* **1989**, *1*, 3489.

(25) Cappa, C. D.; Smith, J. D.; Messer, B. M.; Cohen, R. C.; Saykally, R. J. Effects of Cations on the Hydrogen Bond Network of Liquid Water: New Results from X-Ray Absorption Spectroscopy of Liquid Microjets. *J. Phys. Chem. B* **2006**, *110*, 5301−5309.

(26) Omta, A. W.; Kropman, M. F.; Woutersen, S.; Bakker, H. J. Influence of Ions on the Hydrogen-Bond Structure in Liquid Water. *J. Chem. Phys.* **2003**, *119*, 12457−12461.

(27) Ji, M.; Gaffney, K. J. Orientational Relaxation Dynamics in Aqueous Ionic Solution: Polarization-Selective Two-Dimensional Infrared Study of Angular Jump-Exchange Dynamics in Aqueous 6m $NaClO_4$. *J. Chem. Phys.* **2011**, *134*, No. 044516.

(28) Giammanco, C. H.; Wong, D. B.; Fayer, M. D. Water Dynamics in Divalent and Monovalent Concentrated Salt Solutions. *J. Phys. Chem. B* **2012**, *116*, 13781−13792.

(29) Roget, S. A.; Carter-Fenk, K. A.; Fayer, M. D. Water Dynamics and Structure of Highly Concentrated LiCl Solutions Investigated Using Ultrafast Infrared Spectroscopy. *J. Am. Chem. Soc.* **2022**, *144*, 4233−4243.

(30) Park, S.; Ji, M.; Gaffney, K. J. Ligand Exchange Dynamics in Aqueous Solution Studied with 2DIR Spectroscopy. *J. Phys. Chem. B* **2010**, *114*, 6693−6702.

(31) Sun, Z.; Zhang, W.; Ji, M.; Hartsock, R.; Gaffney, K. J. Contact Ion Pair Formation between Hard Acids and Soft Bases in Aqueous Solutions Observed with 2DIR Spectroscopy. *J. Phys. Chem. B* **2013**, *117*, 15306−15312.

(32) Sun, Z.; Zhang, W.; Ji, M.; Hartsock, R.; Gaffney, K. J. Aqueous Mg^{2+} and Ca^{2+} Ligand Exchange Mechanisms Identified with 2DIR Spectroscopy. *J. Phys. Chem. B* **2013**, *117*, 12268−12275.

(33) Yuan, R.; Fayer, M. D. Dynamics of Water Molecules and Ions in Concentrated Lithium Chloride Solutions Probed with Ultrafast 2D IR Spectroscopy. *J. Phys. Chem. B* **2019**, *123*, 7628−7639.
(34) Yuan, R.; Yan, C.; Fayer, M. Ion−Molecule Complex Dissociation and Formation Dynamics in LiCl Aqueous Solutions from 2D IR Spectroscopy. *J. Phys. Chem. B* **2018**, *122*, 10582−10592.
(35) Yamada, S. A.; Thompson, W. H.; Fayer, M. D. Water-Anion Hydrogen Bonding Dynamics: Ultrafast IR Experiments and Simulations. *J. Chem. Phys.* **2017**, *146*, 234501.
(36) Suydam, I. T.; Boxer, S. G. Vibrational Stark Effects Calibrate the Sensitivity of Vibrational Probes for Electric Fields in Proteins. *Biochemistry* **2003**, *42*, 12050−12055.
(37) Hung, S. T.; Yamada, S. A.; Zheng, W.; Fayer, M. D. Ultrafast Dynamics and Liquid Structure in Mesoporous Silica: Propagation of Surface Effects in a Polar Aprotic Solvent. *J. Phys. Chem. B* **2021**, *125*, 10018−10034.
(38) Shin, J. Y.; Wang, Y.-L.; Yamada, S. A.; Hung, S. T.; Fayer, M. D. Imidazole and 1-Methylimidazole Hydrogen Bonding and Nonhydrogen Bonding Liquid Dynamics: Ultrafast IR Experiments. *J. Phys. Chem. B* **2019**, *123*, 2094−2105.
(39) Yamada, S. A.; Shin, J. Y.; Thompson, W. H.; Fayer, M. D. Water Dynamics in Nanoporous Silica: Ultrafast Vibrational Spectroscopy and Molecular Dynamics Simulations. *J. Phys. Chem. C* **2019**, *123*, 5790−5803.
(40) Yamada, S. A.; Bailey, H. E.; Tamimi, A.; Li, C.; Fayer, M. D. Dynamics in a Room-Temperature Ionic Liquid from the Cation Perspective: 2D IR Vibrational Echo Spectroscopy. *J. Am. Chem. Soc.* **2017**, *139*, 2408−2420.
(41) Matwiyoff, N. A.; Taube, H. Direct Determination of the Solvation Number of Magnesium (II) Ion in Water, Aqueous Acetone, and Methanolic Acetone Solutions. *J. Am. Chem. Soc.* **1968**, *90*, 2796−2800.
(42) Fratiello, A.; Lee, R. E.; Nishida, V. M.; Schuster, R. E. Proton Magnetic Resonance Coordination Number Study of Al(III), Be(II), Ga(III), In(III), and Mg(II) in Water and Aqueous Solvent Mixtures. *J. Chem. Phys.* **1968**, *48*, 3705−3711.
(43) Pálinkás, G.; Radnai, T. Hydration Shell Structures in an $MgCl_2$ Solution from X-Ray and MD Studies. *Z. Naturforsch., A: Phys. Sci.* **1982**, *37*, 1049−1060.
(44) Bleuzen, A.; Pittet, P.-A.; Helm, L.; Merbach, A. E. Water Exchange on Magnesium(II) in Aqueous Solution: A Variable Temperature and Pressure ^{17}O NMR Study. *Magn. Reson. Chem.* **1997**, *35*, 765−773.
(45) Kinosita, K., Jr.; Kawato, S.; Ikegami, A. A Theory of Fluorescence Polarization Decay in Membranes. *Biophys. J.* **1977**, *20*, 289−305.
(46) Lipari, G.; Szabo, A. Effect of Librational Motion on Fluorescence Depolarization and Nuclear Magnetic Resonance Relaxation in Macromolecules and Membranes. *Biophys. J.* **1980**, *30*, 489−506.
(47) Szabo, A.; Lipari, G. Model-Free Approach to the Interpretation of Nuclear Magnetic Resonance Relaxation in Macromolecules. 1. Theory and Range of Validity. *J. Am. Chem. Soc.* **1982**, *104*, 4546−4559.
(48) Tan, H.-S.; Piletic, I. R.; Fayer, M. D. Orientational Dynamics of Water Confined on a Nanometer Length Scale in Reverse Micelles. *J. Chem. Phys.* **2005**, *122*, 174501.
(49) Larentzos, J. P.; Criscenti, L. J. A Molecular Dynamics Study of Alkaline Earth Metal− Chloride Complexation in Aqueous Solution. *J. Phys. Chem. B* **2008**, *112*, 14243−14250.
(50) Soniat, M.; Hartman, L.; Rick, S. W. Charge Transfer Models of Zinc and Magnesium in Water. *J. Chem. Theory Comput.* **2015**, *11*, 1658−1667.
(51) Karthick Kumar, S. K.; Tamimi, A.; Fayer, M. D. Comparisons of 2D IR Measured Spectral Diffusion in Rotating Frames Using Pulse Shaping and in the Stationary Frame Using the Standard Method. *J. Chem. Phys.* **2012**, *137*, 184201.
(52) Shim, S.-H.; Strasfeld, D. B.; Fulmer, E. C.; Zanni, M. T. Femtosecond Pulse Shaping Directly in the Mid-IR Using Acousto-Optic Modulation. *Opt. Lett.* **2006**, *31*, 838−840.
(53) Shim, S.-H.; Zanni, M. T. How to Turn Your Pump−Probe Instrument into a Multidimensional Spectrometer: 2D IR and Vis Spectroscopies Via Pulse Shaping. *Phys. Chem. Chem. Phys.* **2009**, *11*, 748−761.
(54) Tokmakoff, A. Orientational Correlation Functions and Polarization Selectivity for Nonlinear Spectroscopy of Isotropic Media. I. Third Order. *J. Chem. Phys.* **1996**, *105*, 1−12.
(55) Tan, H.-S.; Piletic, I. R.; Fayer, M. D. Polarization Selective Spectroscopy Experiments: Methodology and Pitfalls. *J. Opt. Soc. Am. B* **2005**, *22*, 2009−2017.
(56) Park, S.; Kwak, K.; Fayer, M. D. Ultrafast 2D-IR Vibrational Echo Spectroscopy: A Probe of Molecular Dynamics. *Laser Phys. Lett.* **2007**, *4*, 704.
(57) Hamm, P.; Zanni, M. T. *Concepts and Methods of 2D Infrared Spectroscopy*; Cambridge University Press: New York, 2011.
(58) Schultz, P. W. Ab Initio Calculations of Ionic and Hydrogen Bonding Interactions with the OCN^-, SCN^- and $SeCN^-$ Anions. *Mol. Phys.* **1996**, *88*, 217−246.
(59) Millero, F. J.; Fernandez, M.; Vinokurova, F. Transitions in the Speed of Sound in Concentrated Aqueous Electrolyte Solutions. *J. Phys. Chem.* **1985**, *89*, 1062−1064.
(60) Monnin, C. Densities and Apparent Molal Volumes of Aqueous $CaCl_2$ and $MgCl_2$ Solutions. *J. Solution Chem.* **1987**, *16*, 1035−1048.
(61) Kramer, P. L.; Giammanco, C. H.; Fayer, M. D. Dynamics of Water, Methanol, and Ethanol in a Room Temperature Ionic Liquid. *J. Chem. Phys.* **2015**, *142*, 212408.
(62) Kenkre, V. M.; Tokmakoff, A.; Fayer, M. D. Theory of Vibrational Relaxation of Polyatomic Molecules in Liquids. *J. Chem. Phys.* **1994**, *101*, 10618−10629.
(63) Lenchenkov, V.; She, C.; Lian, T. Vibrational Relaxation of CN Stretch of Pseudo-Halide Anions (OCN^-, SCN^-, and $SeCN^-$) in Polar Solvents. *J. Phys. Chem. B* **2006**, *110*, 19990−19997.
(64) Rey, R.; Hynes, J. T. Vibrational Phase and Energy Relaxation of CN^- in Water. *J. Chem. Phys.* **1998**, *108*, 142−153.
(65) Lee, M. W.; Meuwly, M. On the Role of Nonbonded Interactions in Vibrational Energy Relaxation of Cyanide in Water. *J. Phys. Chem. A* **2011**, *115*, 5053−5061.
(66) Moilanen, D. E.; Fenn, E. E.; Lin, Y.-S.; Skinner, J. L.; Bagchi, B.; Fayer, M. D. Water Inertial Reorientation: Hydrogen Bond Strength and the Angular Potential. *Proc. Natl. Acad. Sci. U. S. A.* **2008**, *105*, 5295−5300.
(67) Roget, S. A.; Kramer, P. L.; Thomaz, J. E.; Fayer, M. D. Bulk-Like and Interfacial Water Dynamics in Nafion Fuel Cell Membranes Investigated with Ultrafast Nonlinear IR Spectroscopy. *J. Phys. Chem. B* **2019**, *123*, 9408−9417.
(68) Sension, R. J.; Hochstrasser, R. M. Comment On: Rotational Friction Coefficients for Ellipsoids and Chemical Molecules with Slip Boundary Conditions. *J. Chem. Phys.* **1993**, *98*, 2490−2490.
(69) Youngren, G. K.; Acrivos, A. Rotational Friction Coefficients for Ellipsoids and Chemical Molecules with the Slip Boundary Condition. *J. Chem. Phys.* **1975**, *63*, 3846−3848.
(70) Moog, R. S.; Ediger, M. D.; Boxer, S. G.; Fayer, M. D. Viscosity Dependence of the Rotational Reorientation of Rhodamine B in Mono- and Polyalcohols. Picosecond Transient Grating Experiments. *J. Phys. Chem.* **1982**, *86*, 4694−4700.
(71) Perrin, F. Mouvement Brownien D'un Ellipsoide-I. Dispersion Diélectrique Pour Des Molécules Ellipsoidales. *J. Phys. Radium* **1934**, *5*, 497−511.
(72) Hu, C. M.; Zwanzig, R. Rotational Friction Coefficients for Spheroids with the Slipping Boundary Condition. *J. Chem. Phys.* **1974**, *60*, 4354−4357.
(73) Hayduk, W.; Cheng, S. C. Review of Relation between Diffusivity and Solvent Viscosity in Dilute Liquid Solutions. *Chem. Eng. Sci.* **1971**, *26*, 635−646.
(74) Evans, D. F.; Tominaga, T.; Davis, H. T. Tracer Diffusion in Polyatomic Liquids. *J. Chem. Phys.* **1981**, *74*, 1298−1305.

https://doi.org/10.1021/acs.jpcb.3c00300
J. Phys. Chem. B 2023, 127, 3278−3290

(75) Nishiyama, Y.; Fukuda, M.; Terazima, M.; Kimura, Y. Study of the Translational Diffusion of the Benzophenone Ketyl Radical in Comparison with Stable Molecules in Room Temperature Ionic Liquids by Transient Grating Spectroscopy. *J. Chem. Phys.* **2008**, *128*, 164514.
(76) Tamimi, A.; Fayer, M. D. Ionic Liquid Dynamics Measured with 2D IR and IR Pump−Probe Experiments on a Linear Anion and the Influence of Potassium Cations. *J. Phys. Chem. B* **2016**, *120*, 5842−5854.
(77) Burgess, J. *Metal Ions in Solution*; Ellis Horwood: Sussex, England, 1978.
(78) Giammanco, C. H.; Kramer, P. L.; Yamada, S. A.; Nishida, J.; Tamimi, A.; Fayer, M. D. Carbon Dioxide in an Ionic Liquid: Structural and Rotational Dynamics. *J. Chem. Phys.* **2016**, *144*, 104506.
(79) Kramer, P. L.; Nishida, J.; Fayer, M. D. Separation of Experimental 2D IR Frequency-Frequency Correlation Functions into Structural and Reorientation-Induced Contributions. *J. Chem. Phys.* **2015**, *143*, 124505.
(80) Kramer, P. L.; Nishida, J.; Giammanco, C. H.; Tamimi, A.; Fayer, M. D. Observation and Theory of Reorientation-Induced Spectral Diffusion in Polarization-Selective 2D IR Spectroscopy. *J. Chem. Phys.* **2015**, *142*, 184505.
(81) Zheng, J.; Kwak, K.; Asbury, J.; Chen, X.; Piletic, I. R.; Fayer, M. D. Ultrafast Dynamics of Solute-Solvent Complexation Observed at Thermal Equilibrium in Real Time. *Science* **2005**, *309*, 1338−1343.
(82) Pye, C. C.; Rudolph, W. W. An Ab Initio and Raman Investigation of Magnesium (II) Hydration. *J. Phys. Chem. A* **1998**, *102*, 9933−9943.
(83) Kwak, K.; Park, S.; Finkelstein, I. J.; Fayer, M. D. Frequency-Frequency Correlation Functions and Apodization in Two-Dimensional Infrared Vibrational Echo Spectroscopy: A New Approach. *J. Chem. Phys.* **2007**, *127*, 124503.
(84) Kwak, K.; Rosenfeld, D. E.; Fayer, M. D. Taking Apart the Two-Dimensional Infrared Vibrational Echo Spectra: More Information and Elimination of Distortions. *J. Chem. Phys.* **2008**, *128*, 204505.
(85) Hoffman, D. J.; Fayer, M. D. CLS Next Gen: Accurate Frequency−Frequency Correlation Functions from Center Line Slope Analysis of 2D Correlation Spectra Using Artificial Neural Networks. *J. Phys. Chem. A* **2020**, *124*, 5979−5992.
(86) Kubo, R. *Fluctuation, Relaxation and Resonance in Magnetic Systems*; Oliver and Boyd: London, 1961.
(87) Asbury, J. B.; Steinel, T.; Stromberg, C.; Corcelli, S. A.; Lawrence, C. P.; Skinner, J. L.; Fayer, M. D. Water Dynamics: Vibrational Echo Correlation Spectroscopy and Comparison to Molecular Dynamics Simulations. *J. Phys. Chem. A* **2004**, *108*, 1107−1119.
(88) Asbury, J. B.; Steinel, T.; Kwak, K.; Corcelli, S. A.; Lawrence, C. P.; Skinner, J. L.; Fayer, M. D. Dynamics of Water Probed with Vibrational Echo Correlation Spectroscopy. *J. Chem. Phys.* **2004**, *121*, 12431−12446.
(89) Bailey, H. E.; Wang, Y.-L.; Lynch, S. R.; Fayer, M. D. Dynamics and Microstructures of Nicotine/Water Binary Mixtures near the Lower Critical Solution Temperature. *J. Phys. Chem. B* **2018**, *122*, 9538−9548.
(90) Zhang, R.; Zhuang, W. Cation Effect in the Ionic Solution Optical Kerr Effect Measurements: A Simulation Study. *J. Chem. Phys.* **2014**, *140*, No. 054507.
(91) Zhang, R.; Zhuang, W. Effect of Ion Pairing on the Solution Dynamics Investigated by the Simulations of the Optical Kerr Effect and the Dielectric Relaxation Spectra. *J. Phys. Chem. B* **2013**, *117*, 15395−15406.

https://doi.org/10.1021/acs.jpcb.3c00300
J. Phys. Chem. B 2023, 127, 3278−3290